GASP. XXII. The Molecular Gas Content of the JW100 Jellyfish Galaxy at $z \sim 0.05$: Does Ram Pressure Promote Molecular Gas Formation?

Alessia Moretti[1] , Rosita Paladino[2] , Bianca M. Poggianti[1] , Paolo Serra[3] , Elke Roediger[4] , Marco Gullieuszik[1] ,
Neven Tomičić[1] , Mario Radovich[1] , Benedetta Vulcani[1] , Yara L. Jaffé[5] , Jacopo Fritz[6] , Daniela Bettoni[1] ,
Mpati Ramatsoku[3,7,8] , and Anna Wolter[9]

[1] INAF-Padova Astronomical Observatory, Vicolo dell'Osservatorio 5, I-35122 Padova, Italy; alessia.moretti@inaf.it
[2] INAF-Istituto di Radioastronomia, via P. Gobetti 101, I-40129 Bologna, Italy
[3] INAF-Cagliari Astronomical Observatory, Via della Scienza 5, I-09047 Selargius (CA), Italy
[4] E. A. Milne Centre for Astrophysics, Department of Physics and Mathematics, University of Hull, Hull, HU6 7RX, UK
[5] Instituto de Fisica y Astronomia, Universidad de Valparaiso, Avda. Gran Bretana 1111 Valparaiso, Chile
[6] Instituto de Radioastronomia y Astrofisica, UNAM, Campus Morelia, AP 3-72, CP 58089, Mexico
[7] Department of Physics and Electronics, Rhodes University, P.O. Box 94, Makhanda, 6140, South Africa
[8] South African Radio Astronomy Observatory, 2 Fir Street, Black River Park, Observatory, Cape Town, 7405, South Africa
[9] INAF-Brera Astronomical Observatory, via Brera 28, I-20121 Milano, Italy

Abstract

Within the GASP survey, aimed at studying the effect of ram pressure stripping on star formation quenching in cluster galaxies, we analyze here ALMA observations of the jellyfish galaxy JW100. We find an unexpected large amount of molecular gas ($\sim 2.5 \times 10^{10} M_\odot$), 30% of which is located in the stripped gas tail out to ~ 35 kpc from the galaxy center. The overall kinematics of the molecular gas is similar to the one shown by the ionized gas, but for clear signatures of double components along the stripping direction detected only out to 2 kpc from the disk. The line ratio r_{21} has a clumpy distribution and in the tail can reach large values ($\geqslant 1$), while its average value is low (0.58 with a 0.15 dispersion). All these evidence strongly suggest that the molecular gas in the tail is newly born from stripped H I gas or newly condensed from stripped diffuse molecular gas. The analysis of interferometric data at different scales reveals that a significant fraction ($\sim 40\%$) of the molecular gas is extended over large scales ($\geqslant 8$ kpc) in the disk, and this fraction becomes predominant in the tail ($\sim 70\%$). By comparing the molecular gas surface density with the star formation rate surface density derived from the Hα emission from MUSE data, we find that the depletion time on 1 kpc scale is particularly large (5–10 Gyr) both within the ram-pressure-disturbed region in the stellar disk and in the complexes along the tail.

Unified Astronomy Thesaurus concepts: D galaxies (346); Galaxy clusters (584); Molecular gas (1073); Galaxy evolution (594)

1. Introduction

Numerous studies in recent years have started analyzing with unprecedented spatial resolution the ionized gas emission coming from cluster spiral galaxies showing extended gaseous tails, aiming to probe the effect of cluster-induced interactions on galaxy evolution. The main mechanism acting on a galaxy gas without altering its stellar component is ram pressure stripping (Gunn & Gott 1972), which has been demonstrated indeed to explain fairly well the observed data, despite its simplicity (Jaffé et al. 2015, 2018). The availability of Integral Field Units, such as the MUSE spectrograph at the Very Large Telescope (VLT) (Bacon et al. 2010), has enormously boosted this field of research, allowing the entire extent of galaxy tails to be mapped, either with mosaic pointings for nearby galaxies (Fumagalli et al. 2014; Fossati et al. 2016; Consolandi et al. 2017) or with single pointings for more distant galaxies (Merluzzi et al. 2013; Bellhouse et al. 2017; Fritz et al. 2017; Gullieuszik et al. 2017; Poggianti et al. 2017b; Moretti et al. 2018b). However, to completely characterize the ram pressure stripping phenomenon, a complete mapping of all the other gas phases is mandatory: X-ray tails have been detected so far only in a few nearby ram-pressure-stripped galaxies (Machacek et al. 2005; Sun et al. 2007, 2010), whereas H I tails have been found in nearby cluster galaxies (Kenney et al. 2004; Oosterloo & van Gorkom 2005; Chung et al. 2009; Abramson et al. 2011;

Scott et al. 2018), and also more recently in the GASP JO206 galaxy (Ramatsoku et al. 2019), located at $z \sim 0.05$, where it has been possible to associate a long H I tail to the Hα one.

Cold molecular gas detection in the tail of nearby gas-stripped spiral galaxies is more recent (Jáchym et al. 2014; Verdugo et al. 2015; Jáchym et al. 2017; Lee et al. 2017; Lee & Chung 2018; Moretti et al. 2018a) and was obtained by making use of single-dish telescopes, with a limited spatial resolution. To date, the ESO 137–001 galaxy in the Norma cluster is the only one that has been analyzed using ALMA band 6 data (Jáchym et al. 2019). These observations have allowed the cold gas through the molecular CO(2–1) transition on subkiloparsec scales to be mapped for the first time in a gas-stripped tail.

In Moretti et al. (2018a), we started a campaign devoted to the study of the molecular gas content of gas-stripped galaxies belonging to the GASP survey[10] (Poggianti et al. 2017b) that aims to study the effects of environmental interactions on nearby ($z \sim 0.05$) cluster galaxies. While the main survey is based on a VLT MUSE Large Program (GAs Stripping Phenomena in galaxies with MUSE; P. I. B. Poggianti) that traces the ionized gas components, complementary data sets at different wavelengths are being collected and have started offering a clear view of all the connected gas phases (see also George et al. 2018; T. Deb et al. 2019, in preparation; Ramatsoku et al. 2019).

---

[10] https://web.oapd.inaf.it/gasp/

In particular, in Moretti et al. (2018a) we observed with the APEX telescope four GASP galaxies and detected molecular gas both in the galaxy disks and cospatially with the stripped ionized gas tails. However, while the overall total gas masses are reliable, the APEX beam has a size of $\sim 28''$ at the observed frequency of CO(2–1), and therefore does not allow the cold gas distribution on small scales to be studied.

In order to understand where the cold molecular gas is located and what the origin of this gas is, we therefore collected ALMA interferometric data at ~ 1 kpc resolution for the same galaxies, and we show in this paper the results we have obtained so far by studying the most massive galaxy in the sample, JW100.

Section 2 is dedicated to the ALMA data description of the observations of two carbon monoxide transitions, CO(2–1) and CO(1–0), while Section 3 shows the derivation of the molecular gas morphology and kinematics. Given the availability of both Band 3 and Band 6 observations, we can also quantify the line temperature ratio, r_{21}, in the entire field covered by both CO(2–1) and CO(1–0) observations, as we describe in detail in Section 4. Section 5 contains our estimates of the cold gas mass found in and around JW100, as well as the comparison between the interferometric and single-dish masses. The comparison with MUSE data has finally allowed us for the first time to derive the star formation efficiency (SFE) resolved on ~ 1 kpc scale, both in the disk and in the tail of this ram-pressure-stripped galaxy, and is discussed in Section 6. A summary of our findings and the conclusions are in Section 7. Throughout this paper, we will make use of the standard cosmology $H_0 = 70$ km s^{-1} Mpc^{-1}, $\Omega_M = 0.3$, and $\Omega_\Lambda = 0.7$, which yields $1'' = 1.071$ kpc at the cluster redshift ($z = 0.055$). The galaxy redshift is, instead, $z = 0.06189$. As in the other GASP papers, our stellar masses are calculated adopting a Chabrier (2003) initial mass function (IMF).

2. Observations and Data Reduction

In this paper, we explore the molecular gas distribution of the ram-pressure-stripped galaxy JW100, located in the cluster A2626. We have classified it as a jellyfish galaxy, as its Hα-emitting tail (extending out to at least ~ 35 kpc) is longer than the stellar disk extension. Among the GASP-targeted galaxies, most of those exhibiting such long tails also possess a central active galactic nucleus (AGN; Poggianti et al. 2017a), as does JW100 (see also Radovich et al. 2019).

The MUSE data analysis was performed as described in Poggianti et al. (2017b), and we just recall here that the galaxy has a mass of $\sim 3 \times 10^{11} M_\odot$ (Moretti et al. 2018a) and lies at a projected distance of ~ 86 kpc (0.05 in terms of R_{200}) from the cluster center. The hosting cluster is located at $z \sim 0.055$ and has a velocity dispersion of ~ 650 km s^{-1} (Biviano et al. 2017). The intracluster medium (ICM) temperature is ~ 3.5 keV (Ignesti et al. 2018). The position of the galaxy in the cluster, together with its projected velocity compared with the cluster velocity dispersion ($v/\sigma_{\rm cl} \sim 2.6$), confirms that this galaxy is located where ram pressure should be most efficient, i.e., in the peak stripping region in the phase-space diagram, close to first pericentric passage (Jaffé et al. 2018). A complete multi-wavelength data set has been collected for this galaxy (X, UV, optical, submillimeter), and has led to the careful analysis of its complex baryon cycling (Poggianti et al. 2019b).

The ALMA observations of JW100 have been taken during Cycle 5 (project 2017.1.00496.S), using Band 3 and Band 6 to observe the CO(1–0) and (2–1) transitions, respectively. Both bands have been used in dual polarization mode, centering one spectral window (spw) on the redshifted frequency of the CO transition, 108.645 GHz for CO(1–0) and 217.294 GHz for CO(2–1), and setting three other spw's to observe the continuum. The spw's centered on the CO lines include 1920 channels and provide a spectral resolution of 0.976 MHz, corresponding to a velocity resolution of 3.1 and 1.5 km s^{-1}, respectively.

The ALMA field of view at the average frequencies of the observations is $59.''7$ and $27.''2$, in Band 3 and Band 6, respectively. To cover with homogeneous sensitivity an area of $57'' \times 62''$, necessary to include the main galaxy and the tail, we set mosaics of 7 and 23 pointings, in Band 3 and Band 6, respectively. The 12 m array Band 3 observations were taken in one session, 40 minutes time on source, observing each pointing of the mosaic for 5.8 minutes. Band 6 observations have been taken in two sessions, for a total time on source of 96 minutes, observing each pointing for 4.2 minutes.

A compact configuration of the array with a number of antennas ranging between 43 and 45 was used in both bands. Adopting as a proxy for the longest baseline the 80th percentile of the uv distance and for the shortest baseline the 5th percentile of the uv distance to calculate the maximum recoverable scale (Equation (7.4) and (7.7) in the ALMA Technical Handbook[11]) the actual configurations used provide a resolution and maximum recoverable scale of $0.''98$ and $13.''38$, respectively, in Band 3, and of 0.7 and $7.''5$, in Band 6.

Additional observations with the 7 m ACA array have been obtained in Band 6 to increase the maximum recoverable scale. The primary beam of the ACA at the average frequency of the Band 6 observations is $46.''6$, a 7 point mosaic was used to cover the same area observed with the 12 m array. Each pointing was observed for ~ 1 hr. A number of antennas ranging between 9 and 11 was used, with a 8.9 m shortest baseline, providing a maximum recoverable scale of $\sim 18''$.

The 12 m array and ACA data sets were independently calibrated using the ALMA pipeline (version Pipeline-CASA51-P2-B). The calibrated data were further analyzed with the CASA software (version 5.4.0-7; McMullin & Waters 2007). The continuum was subtracted from the data sets independently using the CASA task *uvcontsub*. A linear fit of the continuum in the visually selected line-free channels of the spw centered on the line emission was calculated in the visibility plane and subtracted from the full spw.

The flux density scale was fixed using observations of J0006–0623 (for ACA observations in Band 6) and J2253 +1608 for the 12 m array observations both in Band 3 and Band 6. We can estimate an uncertainty in the flux measured to be of the order of 10%, including the calibration and clean errors. We checked the accuracy of the ALMA and ACA relative flux scales by comparing the flux on the overlapping spatial scales between the two arrays and found that they are consistent within 10%, which is the calibration uncertainty. The 12 m and ACA visibilities, calibrated and continuum subtracted, were concatenated and used for the deconvolution.

The images of line and continuum emissions in Band 3 and Band 6 were obtained using the CASA task tclean. Continuum images were obtained using the three additional spw's observed, covering a bandwidth of 5.25 GHz using Briggs

---

[11] https://almascience.eso.org/documents-and-tools/latest/alma-technical-handbook

Table 1
Properties of Band 3 and Band 6 ALMA Images: Synthesized Beam (θ_{maj}, θ_{min}, and PA), rms, and Peak of Cleaned Images

	θ_{maj} (arcsec)	θ_{min} (arcsec)	PA (deg)	rms (Jy/beam)	Peak (Jy/beam)
			Band 3		
Cont	1.98	1.72	−1.03	$1.8 \cdot 10^{-5}$	...
CO(1–0)	2	1.7	8.3	$9 \cdot 10^{-4}$	$2.5 \cdot 10^{-2}$
			Band 6		
Cont	1.35	1.08	33.7	$4.4 \cdot 10^{-5}$	$6.7 \cdot 10^{-4}$
CO(2–1)	1.4	1.12	33.04	$8 \cdot 10^{-4}$	$4.2 \cdot 10^{-2}$

Note. Band 6 properties refer to the image obtained combining 12 m and ACA data.

weighting with a robust value of 0.5. In Band 3, there is no continuum emission, while in Band 6 a peak, with signal-to-noise ratio (S/N) 15, located at R.A. 23:36:26 decl. 21:08:54.8, is detected.

The data cubes were obtained by smoothing the spectral resolution to $20 \, \mathrm{km \, s^{-1}}$. The channel velocities were computed in the LSRK velocity frame (radio convention) with a zero point corresponding to the redshifted frequencies of the observed CO transitions (108.644 GHz for the (1–0) and 217.258 for the (2–1)). The continuum-subtracted dirty cubes were cleaned in regions of line emission initially identified automatically (using the automask parameter in tclean) and further refined interactively to better account for possible faint residual emission. The weighting used for the line images was natural, to enhance the sensitivity. The achieved rms was measured in line-free channels of the cubes.

For both continuum and line images, the resulting properties —synthesized beams, peaks, and rms—are reported in Table 1.

In the following analysis, Band 6 data used are obtained by combining 12 m and ACA data.

3. Data Analysis

3.1. Molecular Gas Morphology

Starting from the cleaned data cubes at $20 \, \mathrm{km \, s^{-1}}$ resolution, we constructed a detection mask using the SOFIA software (Serra et al. 2015). In particular, we used SoFiA to remove spatial and spectral noise variations from the data cubes; convolve the data cubes with several 3D smoothing kernels and, for each kernel, apply a detection threshold; and merge detected voxels into 3D objects and reject false detections based on their integrated signal to noise and reliability calculated as Serra et al. (2012).

The first three moment maps are shown in Figure 1. The upper panels show the moment zero, i. e., the integrated line flux along the entire frequency range within the SoFiA masks, both for CO(2–1) and for CO(1–0).

The superimposed green contour shows the stellar disk extent derived from the most external (~1.5σ above background) isophote of the continuum MUSE light under Hα (as in Poggianti et al. 2019b) and in black, only in the CO(1–0) map, the two regions A and B covered by our APEX observations (Moretti et al. 2018a). The temperature scale goes from 0 to 60 K km s^{-1}. The beam size is drawn in red in the lower-left corner of each map. White contours superimposed in both panels are at 1, 3, and 5 moment zero rms (defined as rms = rms(cube) $\times \sqrt{N_{chan} \times \Delta_v}$).

Considering significant every detection of the line emission spread over five channels, i.e., with a line width of $\sim 100 \, \mathrm{km \, s^{-1}}$, the minimum measurable mass that we obtain using the relation given in Equation (1), which we will describe in Section 5, is $\sim 1 \times 10^7 M_\odot$.

The intensity-weighted velocity (moment 1) and dispersion of velocity (moment 2) are shown in the middle and lower panels of Figure 1, respectively, where the CO(2–1) contours are shown in black to guide the eye.

The CO emission appears elongated as the galaxy disk, but it is clearly less extended and displaced toward the west side of the disk, in the same direction as the tail of ionized gas revealed by MUSE and, therefore, of the ram pressure wind. The peak of the CO emission (both CO(2–1) and CO(1–0)) is located northwest with respect to the galaxy nucleus (shown as a red cross in the top panels of Figure 1), at a distance of ~5 kpc. The peak in correspondence of the galaxy center seems to host less CO. A similar missing flux in the central kiloparsec has also been observed in the Andromeda galaxy (Nieten et al. 2006), possibly originating from a satellite passage and in M51 (Schinnerer et al. 2013). Ring-like structures have been found in a few galaxies belonging to the HERACLES survey (Leroy et al. 2009) and in the NGC 613 galaxy (Miyamoto et al. 2017) where the circumnuclear disk also shows a very low SFE.

CO emission is then present in the southwest tail in discrete regions with detected sizes up to ~5 kpc, confirming the APEX detection by Moretti et al. (2018a).

The extent of each individual region is clearly much bigger than the typical size of Milky Way Giant Molecular Clouds (GMCs; Heyer & Dame 2015), but our resolution is such that we cannot exclude that each of them could be made of different unresolved regions. It is remarkable, in any case, that ALMA data confirm the presence of CO emission at such large distances (up to ~35 kpc) from the JW100 main body.

The distributions of CO(2–1) and CO(1–0) are very similar, but not entirely coincident, due to the larger extent of CO(1–0), known to trace a more diffuse emission.

In order to clearly identify the emitting regions, we fitted a 2D Gaussian profile on each of them in the zero-moment CO(2–1) map, shown again with a larger size in Figure 2. This has allowed us to define a number of regions both within the galaxy disk, following the strongest CO concentration (regions D1, D2, and D3 in Figure 2), and the emissions close to the disk itself, but slightly displaced (regions NT1, NT2, and NT3 in Figure 2), as well as the farthest clumps along the tail (regions FT1, FT2, FT3, FT4, and FT5 in Figure 2). The shape, orientation, and size (Gaussian FWHM) of each region are shown in Figure 2 (red ellipses).

The Hα emission, as derived from MUSE data, is shown with colored contours in Figure 2. This emission remarkably traces the CO emission, as expected. However, there is one striking difference that is worth mentioning: the northern tail of Hα has an overlapping CO emission with significant flux only within ~15 kpc from the galaxy center while its southwest extending tail is filled with knots of CO, with elongated shapes. There are also Hα-emitting regions that do not have a molecular gas counterpart, especially in the southwest edge of the distribution but also close to the NT3 region. They are better discussed in Poggianti et al. (2019, accepted). The two Hα concentrations seen northwest and southwest are, instead, foreground stars.
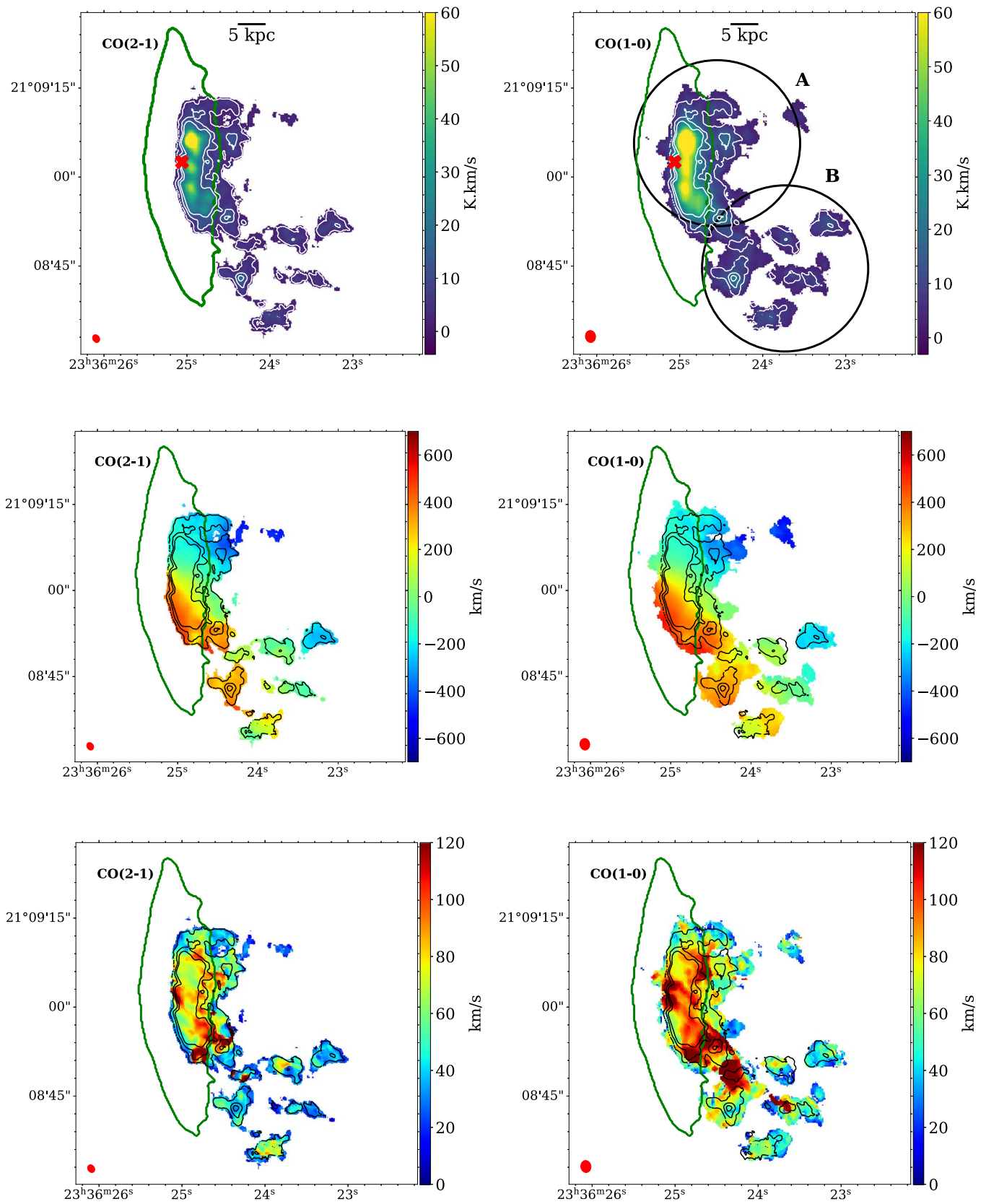
Figure 1. (Upper panels) CO(2–1) and CO(1–0) moments zero from ALMA data, from 0 to 120 K km s^{-1}. Beam sizes are drawn in red in the bottom-left corner. The red cross shows the position of the galaxy center. The two big black circles on the right panel are the original APEX pointings from Moretti et al. (2018a). (Middle, lower panels) CO(2–1) and CO(1–0) first moments and velocity dispersions (in km s^{-1}) from ALMA data. White contours (in the upper panels) and black contours in the others trace CO(2–1) at the 1, 3, and 5 moment zero rms. In all panels, the green contour shows the extent of the stellar disk from MUSE data. In all panels, north is up and east is left.
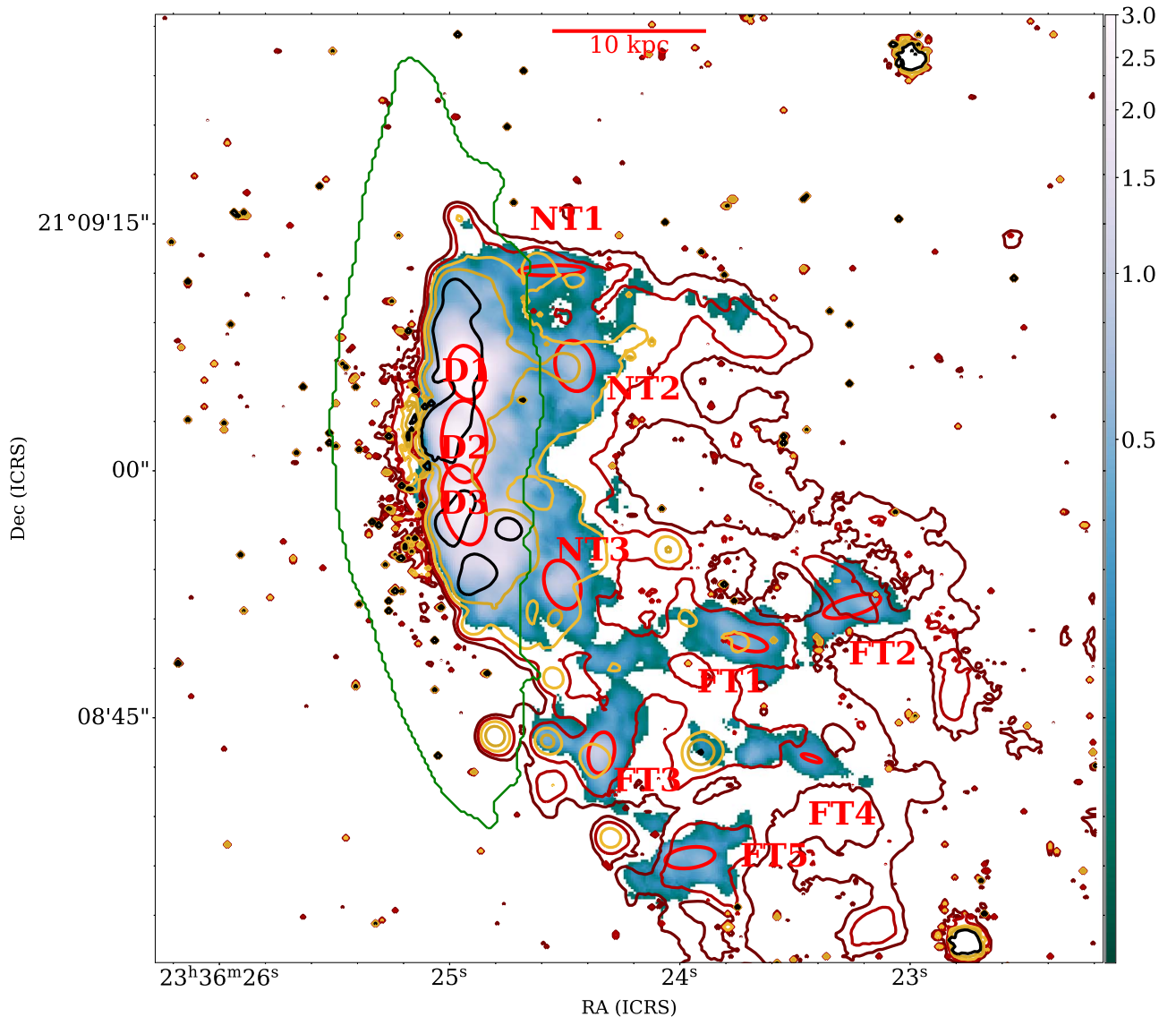
Figure 2. CO(2–1) emission (in Jy/beam km s^{-1}) map of JW100 with superimposed the Hα contours from MUSE (in different colors, at 2×10^{-17}, 4×10^{-17}, 8×10^{-17}, 1.6×10^{-16}, and 3.2×10^{-15} erg cm^{-2} s^{-1} arcsec^{-2}) and the regions analyzed in this paper in red (labels D1 to D3 for the disk regions, NT1 to NT3 for the clumps close to the disk, and FT1 to FT5 for the clumps in the far tail). The green contour shows the extent of the stellar disk.

ALMA data reveal therefore the presence of large clumps of molecular gas well beyond the extent of the galaxy disk, thus posing an important challenge to explain its origin: is this molecular gas being stripped from the galaxy due to the ram pressure, or is it formed in situ from the stripped neutral gas that has been able to cool down and is now prone to form new stars? In order to answer this question, we further analyze the line-of-sight velocity of the molecular gas as revealed by the first moment of ALMA data.

3.2. Molecular Gas Kinematics

From the first-moment maps, it can be seen that the two CO emission lines are broadly cospatial (but the southwest tails show more concentrated CO(2–1) knots) and show similar velocities in the regions close to the galaxy disk. It has to be noted, though, that first moments are intensity weighted and therefore trace the motion of the summed components, in case of double-peaked emission. APEX spectra within the two broad A and B regions have shown that the molecular gas is rotating

following the rotation of the ionized gas in the galaxy disk both in the central region and in the tail (hence the double-peak emission), and ALMA data extracted from the same region confirm this results.

In order to better compare the cold molecular gas with the ionized gas motions, we constructed a velocity channel map by cutting the MUSE data cube around the Hα emission[12] in the same velocity range covered by ALMA observations and rebinning the ALMA data to match the MUSE velocity resolution (a dedicated cube with the same velocity resolution and pixel size of the MUSE data was produced for this purpose).

Overall, we can see from Figure 3 that the molecular gas broadly follows the ionized gas emission, i.e., consistent with the Hα velocity field, the molecular gas in the tail retains a memory of the disk rotation. However, as observed in Hα, the

---

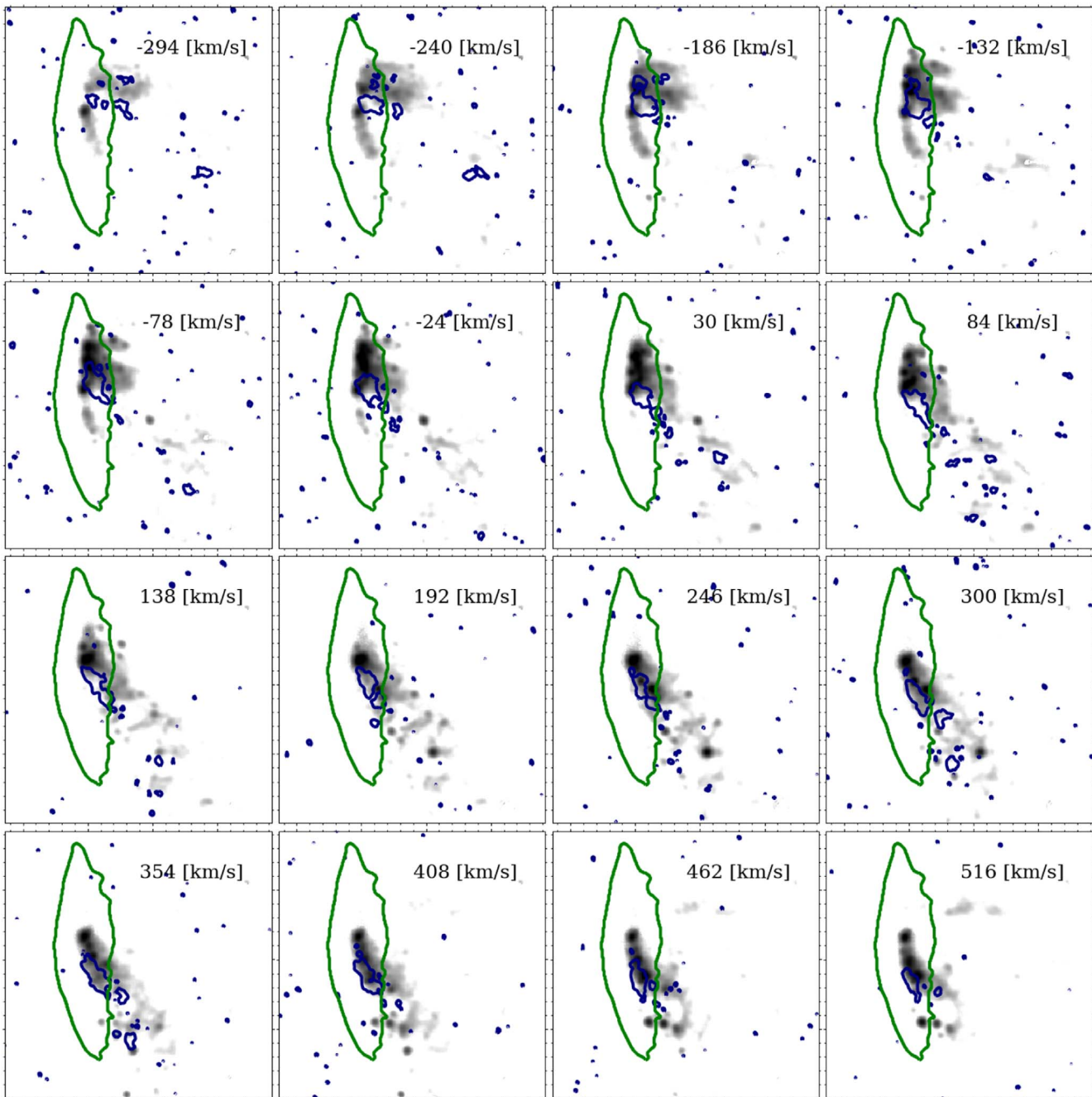[12] Unfortunately, the Hα line is somewhat contaminated by the contiguous N II lines.

Figure 3. Velocity channel map showing the Hα emission at different velocities, with the contour of the CO(2–1) emission from ALMA data superimposed in blue. The field of view of each plot corresponds to the one shown in the other figures of the paper.

CO also exhibits a decrease in the line-of-sight velocity as the distance from the disk increases westward.

A comprehensive characterization of the galaxy kinematics is beyond the scope of this paper and will be analyzed in a forthcoming study. Here, however, we aim to understand the broad characteristics of the cold gas behavior as revealed by ALMA.

Given that the Hα emission of JW100 shows a double component (Poggianti et al. 2017a), we tried to understand whether the molecular gas shows the same behavior, by using a multi-Gaussian fitting of the CO line emission on each pixel above the 3σ level. We have used the gausspy+ code, which automatically evaluates the number of Gaussians needed to fit a spectrum through subsequent refinements that take into account

the presence of blended or broad components (Riener et al. 2019). We found that in some regions, mostly within the galaxy disk, the CO(2–1) line needs to be fitted using two Gaussians, even with the ALMA-enhanced spatial resolution (yellow regions in Figure 4). Fitting the CO(2–1) emission with only one Gaussian would produce artificially high velocity dispersion values (as can be seen in the lowest panels of Figure 1). The few spaxels where a third component is needed are not coincident with the AGN position (marked with a red cross).

The two components within the galaxy disk and in its vicinity (up to 1–2 kpc from it) are well explained if we think that one is associated with the gas rotating in the disk and the second (the less dense one) is being stripped due to the ram pressure. The CO(2–1) emission in the tail regions can be fitted
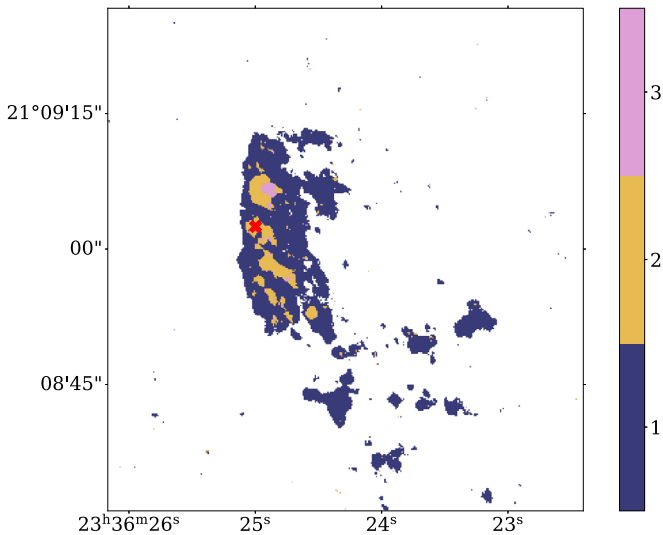
Figure 4. Number of Gaussians needed to fit the CO(2–1) line emission from ALMA+ACA data. The red cross marks the AGN position.

instead with one single Gaussian, and can be either born in situ, or stripped as well. In this last case, though, we expect it to be characterized by a low density, as this component should be more easily stripped. We will try in Section 4 to assess this point by estimating the molecular gas density through the r_{21} ratio.

The rotation of the molecular gas in the disk while ram pressure is in action can also explain the accumulation of molecular gas in the D1 region, as all disk gas at the upstream edge that is pushed back by the ram pressure passes through it. If this is the case, multiple kinematics components are also not surprising. The cold gas motion could be in fact slowed down by the overall motion of the galaxy within the ICM, which would result in accumulation of approaching (blueshifted) gas if the galaxy is falling toward us and, therefore, the ram pressure wind component along the line of sight points away from us. The receding (redshifted) gas on the other side would be more easily removed, as the southern tail demonstrates.

Molecular gas outflows have been detected nowadays in many nearby active galaxies but they extend on smaller spatial scales and show clear high-velocity wings, which we cannot see in our data (Cicone et al. 2014; Feruglio et al. 2015). The northern D1 region, though, is far from the galaxy center (∼5 kpc), and it also has a different orientation with respect to the outflow shown by the ionized gas (Radovich et al. 2019), and we therefore think it is not due to a massive outflow.

In order to understand the cold gas rotation, we extracted from the masked CO(2–1) cube a generous slit 20″ long and 9″ wide, centered on the galaxy center, in the south–north direction with a position angle (PA) of 0°.66 (shown in Figure 5) and produced the position–velocity (PV) diagram shown in the right panel of the same figure. We choose a wide slit width in order to include the bright CO emission west of the center while still centering the slit on the galaxy itself. However, the PV diagram does not change significantly if we use an offset, narrower slit with the same PA and centered on the bright CO emission.

By comparing the left and right panels, it is easily seen that the CO distribution is concentrated in the three regions D1, D2, and D3 described above.

The PV diagram along the major axis of a nearly edge-on, massive galaxy should be characterized by a broad S shape (in velocity), due to the quickly rising rotation curve (e.g., Noordermeer et al. 2007) and to the fact that at any given position along the extracted slit, many components of the rotating disk should be intercepted. The rising part of the diagram should reach a maximum (at about 1 kpc) and then flatten. In our case, though, the gas shows a more linear behavior, meaning that either some gas is missing from the central ∼3 kpc, as is the case if it is distributed within a ring, or that the rotation curve is still slowly rising at a radius of 3 kpc, which would be unusual for a galaxy of this mass.

It also suggests that there might be two different slopes, one tracing the rotation of the CO in regions D1 and D3, and a second steeper one in the central region D2, which also shows a discontinuity at both edges, possibly marking the extent of a ring. This possible secondary component could be due to the presence of a bar (Funes et al. 2002; Kuzio de Naray et al. 2009) and the fact that the peak of the CO is displaced with respect to the center of this presumed bar is not totally unexpected (Sorai et al. 2000; Kuno et al. 2007) and might trace a bar evolutionary sequence (Jogee et al. 2005; Sheth et al. 2005).

As seen above, the CO kinematics shows two peaks in many regions within the galaxy disk. This helps in understanding the second-moment maps, where the galaxy disk and region NT3 show a large velocity dispersion. All the CO regions along the stripped tail have low velocity dispersions ($\leqslant 40\,\mathrm{km\,s^{-1}}$), typical of star-forming regions, as shown in the bottom panels of Figure 1.

4. H$_2$ from Different Isotopes: Deriving the R21

Given the complex environment in which JW100 resides, and in particular its position within an extremely disturbed cluster (Gitti 2013; Ignesti et al. 2017, 2018), we can expect that the physical conditions among the detached knots of emitting CO will be different, as is different the surrounding ICM. Moreover, as previously noted by Poggianti et al. (2019), most of the Hα-emitting knots detected with MUSE are characterized by optical line ratios typical of star-forming regions, but some of them appear powered by shocks if using other line ratios.

Using ALMA data, and in particular the r_{21} brightness temperature line ratio ($r_{21} \equiv T_{21}/T_{10}$, where the temperature comes from the CO-emitting lines), we can now characterize the physical conditions of the molecular gas. This ratio is sensitive to both the density and the temperature structure of the gas, as well as the optical depth of the two lines. Studies on the resolved GMCs in Orion (Nishimura et al. 2015) have revealed that the inner portions of a GMC has usually $r_{21} = 1$ and then declines outward, reaching $r_{21} \sim 0.5$.

We therefore constructed the r_{21} map using the ALMA data as follows: we first masked the CO(2–1) and the CO(1–0) cubes at $20\,\mathrm{km\,s^{-1}}$ resolution, as described in Section 3.1; then, we smoothed the CO(2–1) data cube with a Gaussian kernel to get an image with the same beam as the CO(1–0) beam and regrid it on the CO(1–0) one; we finally extracted the ratio between the two zero-moment maps (which gives the integrated brightness temperature ratio, hereafter the r_{21} line ratio), which is shown in Figure 6, top panel. Clearly, this value could be derived only when both measurements are available. The lower panel shows, instead, the distribution of the r_{21} ratio, in blue for all pixels
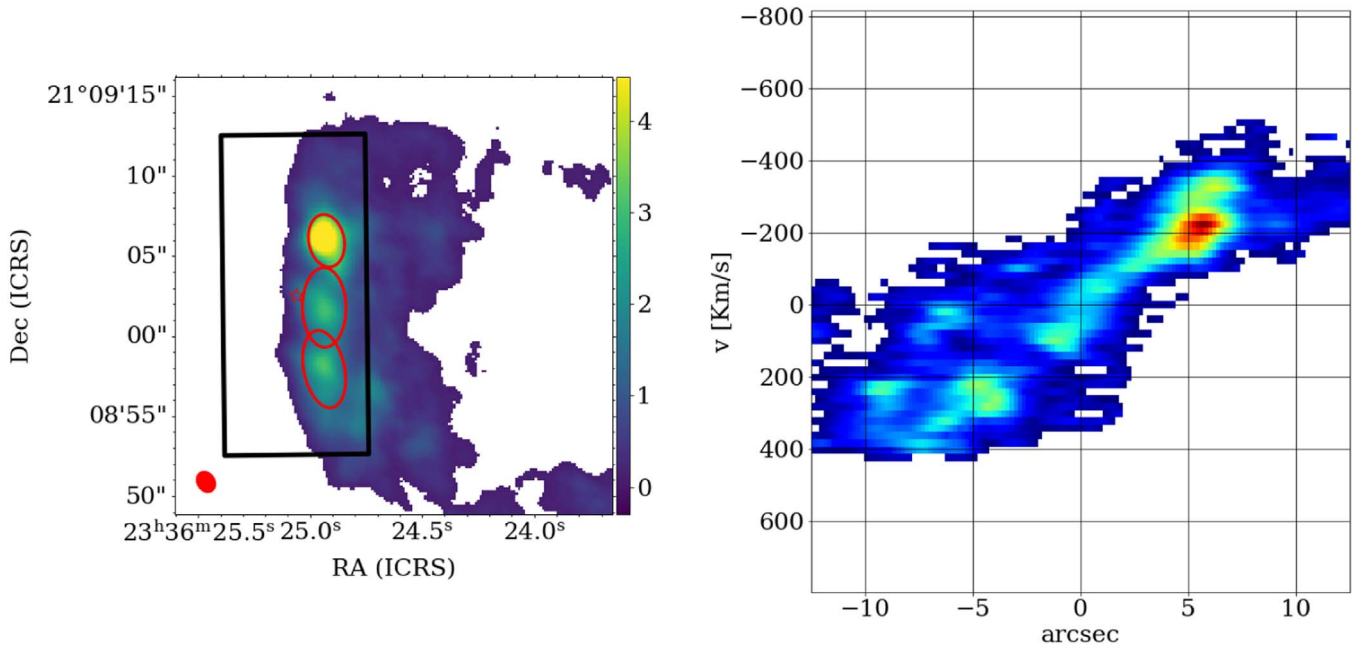
Figure 5. In the left panel, the black box shows the $20'' \times 9''$ wide slit from which we extracted the position–velocity diagram shown in the right panel. Red ellipses show the position of the D1, D2, and D3 regions described in the text.

where the measurement has been possible, in red for the disk region only.

The r_{21} distribution is very clumpy and goes from 0.1 to ~ 1 in the galaxy disk, while higher values (~ 1.5) are found in the tail.

A Gaussian fit of the distribution (shown in green in the lower panel of Figure 6) finds an average value of $\sim 0.58 \pm 0.15$ in the galaxy disk, which is lower than the usually adopted value of ~ 0.8 (Leroy et al. 2009; Saintonge et al. 2017) that we also used in the analysis of APEX data. The value that we find is compatible with the one found in nearby resolved studies of star-forming disks (Leroy et al. 2013). Extremely high values are found in galaxy nuclei, which can reach $r_{21} \sim 1$, (Leroy et al. 2009), while the lower tail of values at ~ 0.3 has been interpreted as due to optically thin, subthermally excited CO in warm ($T > 40$ K), diffuse ($n < 10^3$ cm^{-3}) regions of single simulated clouds (Peñaloza et al. 2017). Similar values have also been reported in the outskirts of the Orion region (Nishimura et al. 2015).

In JW100, besides the low average value, the distribution appears very clumpy both in the disk and in the tail. In particular, small regions of $r_{21} \geqslant 1$ are found in the stripped tail, but they are not spatially coincident with the peaks of the CO emission defining the regions described above, nor with the peaks of the Hα emission. As discussed in Poggianti et al. (2019, accepted), this can be due to evolutionary effects related to the star formation process.

The estimated mean value found in every analyzed region is reported in column 9 of Table 3 together with its error (standard deviation).

Our r_{21} determinations confirm that within the galaxy disk the gas is optically thick and cold (with line ratios lower than 0.8 in the regions called D1, D2, and D3). Region NT1 is characterized by a particularly low value (0.45), which is thought to trace more diffuse and warm gas (~ 40 K), characterized by a very faint emission (Peñaloza et al. 2017). This CO complex lies in fact in the northern region around

JW100, where the X-ray-emitting gas is more concentrated (Poggianti et al., accepted), and might have had the chance to heat the molecular gas. r_{21} increases in clumps located within the farther regions, implying that along the tail, the gas becomes optically thick, being dense and warm. The stripping of such dense clumps out to a distance of ~ 30 kpc from the center of JW100, assuming the typical lifetime found in nearby massive galaxies, i.e., ~ 5 Myr (Chevance et al. 2019), would imply a stripping velocity of ~ 5900 km s^{-1}, which is rather unlikely. Therefore, these dense clouds would be destroyed before reaching the position of the farthest clumps along the tail of JW100, supporting a scenario where molecular gas in the stripped tail is originated in situ.

High values of the r_{21} ratio are usually found in the central regions of galaxies (Casoli & Dupraz 1991; Braine & Combes 1992) where new stars are born. Instead, the D2 region in JW100, which is the closest to the galaxy center, has $r_{21} = 0.62$, possibly because the energetic source here is the central AGN, and not SF.

5. Quantifying the H$_2$ Mass

We now use the molecular gas emission (both the CO(2–1) and the CO(1–0)) to evaluate the total CO fluxes and then derive the molecular gas mass adopting the formulations by Watson & Koda (2017), i.e.,

$$\left(\frac{M_{H_2}}{M_\odot}\right) = 3.8 \times 10^3 \left(\frac{\alpha_{10}}{4.3}\right)\left(\frac{r_{21}}{0.7}\right)^{-1}\left(\int S_{21} dv\right)(D_L)^2 \quad (1)$$

and

$$\left(\frac{M_{H_2}}{M_\odot}\right) = 1.1 \times 10^4 \left(\frac{\alpha_{10}}{4.3}\right)\left(\int S_{10} dv\right)(D_L)^2, \quad (2)$$

where α_{10} is the CO-to-H_2 conversion factor expressed in $M_\odot$ pc^{-2} (Bolatto et al. 2013), r_{21} is the CO $J = 2$–$1/1$–0 line ratio, S_{21} is the CO integrated line flux in Jy, and D_L is the
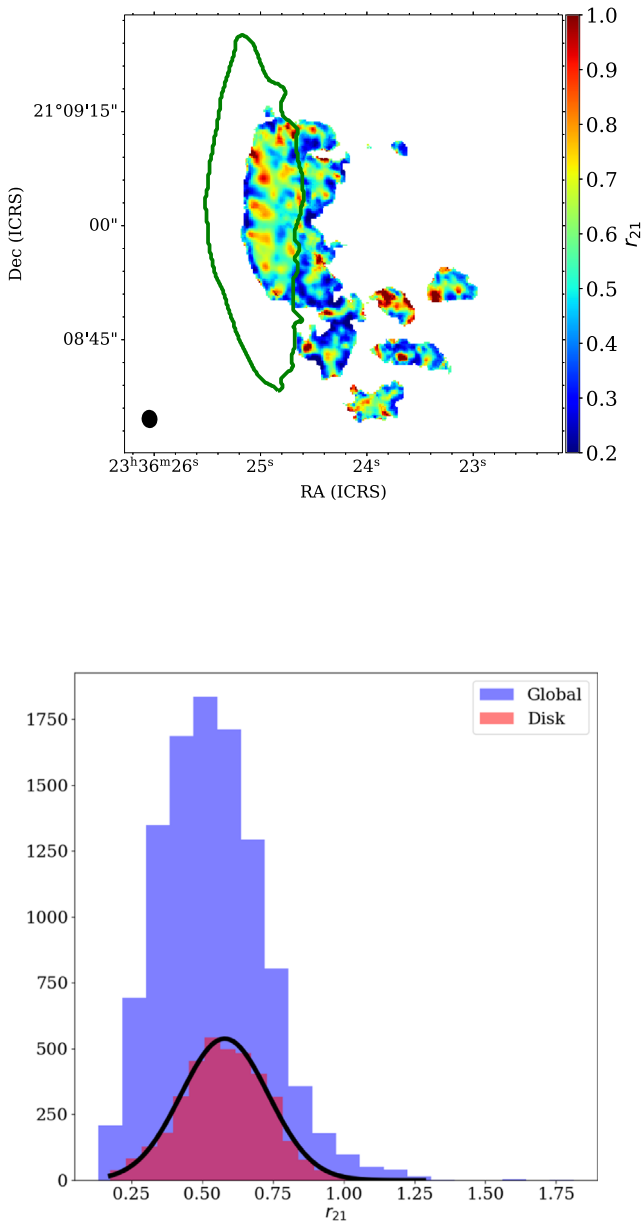
Region	CO Flux (Jy km s^{-1}) 12 m	CO Flux (Jy km s^{-1}) 12 m+ACA	CO Flux (Jy km s^{-1}) APEX
JW100 [A]	63	99	110
JW100 [B]	11	32	36

Note. Column 2 refers to the 12 m observations only and column 3 to the combined interferometric and ACA Data. Column 4 refers to the integrated fluxes of APEX spectra from Moretti et al. (2018a) in the same velocity range as ALMA data.

Figure 6. (Top) r_{21} ratio map with superimposed the galaxy stellar contour (in green). (Bottom) r_{21} distribution for the entire data set (in blue) and for the disk region only (in red). The fit to the disk region is overplotted in black.

luminosity distance in Mpc. Using this formulation or the one from Solomon & Vanden Bout (2005) does not change more than 5% our masses. Throughout this paper, we always use $\alpha_{10} = 4.3$, i.e., the standard Milky Way value corresponding to CO-to-H$_2$ = 2×10^{20} cm^{-2}(K km s^{-1})$^{-1}$ including the helium correction. As for r_{21}, we will use the same value (0.79) that we used in our APEX data analysis for the sake of comparison. We will also estimate the gas masses from CO(2–1) adopting the observed value of r_{21} and the masses from CO(1–0).

A first question we can answer at this point is to what extent the overall H$_2$ mass is compatible with the one measured with the APEX single dish, as with ALMA we might be less sensitive to the largest scales of CO emission. A mismatch between the interferometric flux and the one measured with the single dish is expected. In fact, numerical simulations by Helfer et al. (2002) find that ALMA would recover only ∼75% of the

total flux on large scales, this value being also dependent on the S/N and on the distance from the galaxy center, as confirmed by observations (Helfer et al. 2003).

In order to derive H$_2$ masses, we simply integrated the ALMA spectra within the two A and B regions defined by APEX pointings and performed the same integral on the APEX spectra both within the same velocity range covered by ALMA detections. The results are given in Table 2. Errors on ALMA fluxes amount to ∼10%, while those on APEX data are at least double (Dumke & Mac-Auliffe 2010).

The percentage of flux loss when using the ALMA+ACA combination is similar in the two pointings (∼10%), and compatible with the measurement errors. However, when considering the broader velocity range covered by the APEX spectrum in pointing A, the comparison of the two fluxes reveals the presence (at about ∼1σ level) of a supplementary gas component at high velocity (between 500 and 800 km s^{-1}) that is completely missed by ALMA and ACA observations, which could possibly suggest the presence of diffuse components on large scales.

By integrating the spectra using the 12 m array data only, we miss ∼43% of the flux in the galaxy disk and ∼70% in the tail region.

This means that both in the disk and in the tail, the CO emission is more diffuse than the largest scale recovered by ALMA 12 m, and that ACA is mandatory to recover the total flux. As previously found by Pety et al. (2013), Jáchym et al. (2019), the molecular gas in the tail is therefore more diffuse than that in the disk.

Estimating the total amount of molecular gas within this galaxy has deep consequences on the understanding of the origin of the gas itself: in fact, single-dish surveys (Saintonge et al. 2011), as well as interferometric observations of nearby undisturbed galaxies from CALIFA (Bolatto et al. 2017), give an estimate on the ratio of molecular over stellar mass, which turns out to be ∼0.01 (for stellar masses larger than 10^{11} $M_\odot$), so that for JW100, the expected value of molecular gas is ∼$3 \times 10^9 M_\odot$. The number of massive galaxies for which molecular gas masses are available in Bolatto et al. (2017) is very limited, but none of them reaches ratios larger than 0.02. More massive galaxies are present in the COLDGASS sample (Saintonge et al. 2011), but again, the molecular gas mass ratio never exceeds 6% of the stellar mass.

We find that ALMA data account for a total H$_2$ mass of ∼2.5×10^{10} $M_\odot$.

If we consider as a stellar disk the generous definition that is shown by the green contours in all the maps, we end up with a total molecular gas mass in the galaxy disk of $1.8 \times 10^{10} M_\odot$, while in the tail it amounts to $0.7 \times 10^{10} M_\odot$.

Table 3
CO(2–1) and CO(1–0) Fluxes of Selected Regions (Columns 4 and 7), with the Corresponding H_2 Masses Calculated Using $r_{21} = 0.79$ (Column 5) and the Measured One (Column 6)

Region	R.A.	decl.	CO(2–1) (Jy km s^{-1})	$M(H_2)$ ($10^9 M_\odot$) $r_{21} = 0.79$	$M(H_2)$ ($10^9 M_\odot$) r_{21} = meas	CO(1–0) (Jy km s^{-1})	$M(H_2)$ ($10^9 M_\odot$)	r_{21}
JW100 D1	23:36:24.927	+21:09:05.958	13.34	2.71	3.02	4.46	2.93	0.71 ± 0.11
JW100 D2	23:36:24.937	+21:09:01.784	10.57	2.15	2.74	3.94	2.62	0.62 ± 0.11
JW100 D3	23:36:24.937	+21:08:57.929	9.59	1.95	2.41	3.71	2.46	0.64 ± 0.08
JW100 NT1	23:36:24.556	+21:09:12.173	0.21	0.04	0.07	0.12	0.08	0.45 ± 0.17
JW100 NT2	23:36:24.457	+21:09:06.368	1.79	0.36	0.50	0.76	0.51	0.57 ± 0.09
JW100 NT3	23:36:24.510	+21:08:53.082	1.93	0.39	0.56	0.84	0.56	0.55 ± 0.12
JW100 FT1	23:36:23.710	+21:08:49.577	0.44	0.09	0.10	0.15	0.10	0.69 ± 0.13
JW100 FT2	23:36:23.252	+21:08:51.774	0.53	0.11	0.17	0.27	0.18	0.51 ± 0.11
JW100 FT3	23:36:24.341	+21:08:42.878	1.27	0.26	0.33	0.49	0.32	0.62 ± 0.10
JW100 FT4	23:36:23.429	+21:08:42.543	0.06	0.01	0.01	0.02	0.01	0.69 ± 0.06
JW100 FT5	23:36:23.956	+21:08:36.501	0.61	0.12	0.16	0.23	0.16	0.62 ± 0.09

Note. The r_{21} measured from ALMA data is given in column 9.

The disk value is compatible with the ones found by the HERACLES survey (Leroy et al. 2009) of nearby undisturbed galaxies (which however have lower stellar masses), but is about one order of magnitude larger than the typical molecular gas mass found in galaxies of similar stellar mass in Virgo (Corbelli et al. 2012).

Unfortunately, we could not observe the H I emission of this galaxy with the J-VLA, as was done for other GASP jellyfishes (Ramatsoku et al. 2019; T. Deb et al. 2019, in preparation), due to the presence of radio interference at its redshift. We are currently obtaining MeerKAT observations for this galaxy.

Assuming for this galaxy a normal H I content, i.e., $H_2/H I = 0.3$ (Saintonge et al. 2011), we end up with a total gas fraction of $0.32\times$ the stellar mass, which is 10 times larger than the expected value for galaxies with similar mass at the same redshift (Catinella et al. 2018). In fact, our H_2 mass estimate already provides a molecular-only gas mass fraction of 0.08, i.e., two times larger than the expected value, without accounting for the H I gas. In any case, whatever the contribution of the H I gas, JW100 has a very high content of molecular gas. Similarly high molecular gas fractions have been found also in NGC 3627, a barred interacting and active (LINER) galaxy belonging to the NUGA survey (Casasola et al. 2011) as well as in other interacting galaxies (Kaneko et al. 2017). Active galaxies with similar masses in the xCOLD GASS sample show, instead, lower molecular gas fractions, but they are not ram pressure stripped/disturbed.

For each region defined in Section 3.1, we estimated the CO flux from the integrated spectrum.

Molecular gas in the near-tail regions (NT1, NT2, and NT3) amounts to 1.13×10^9 solar masses, while the far-tail clumps (FT1 to FT5) account for $\sim 0.8 \times 10^9$ solar masses of H_2. These values, though, refer to the small elliptical regions shown in Figure 2, i.e., they do not take into account the more diffuse emission. If we integrate our zero-moment map, instead, we find that outside the disk, $\sim 7 \times 10^9 M_\odot$ of molecular gas are present.

We give in Table 3 the flux (and corresponding mass) of each region while in Figure 7 we show the CO (2–1) flux density within the selected regions.

For each region, we estimated the molecular gas mass from both the CO(2–1) and CO(1–0) fluxes. The two masses are in good agreement when using the appropriate value of r_{21} (see
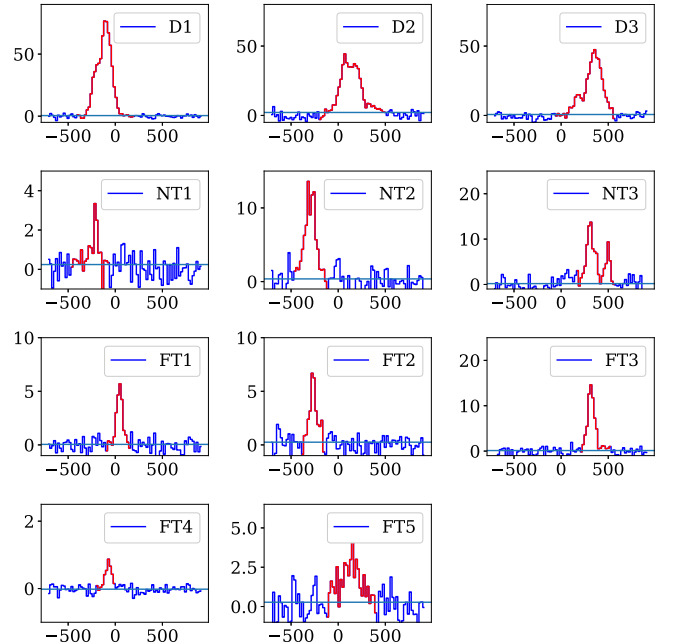

Figure 7. CO(2–1) integrated spectra in the selected regions D1 to FT5 defined in Section 3.1. The red line traces the flux integrated to obtain the molecular gas mass. The blue horizontal line is the median flux density within the region.

Section 4) that we have obtained as the mean value within the analyzed region. The use of the fixed value of r_{21} would provide an underestimation of the amount of molecular gas.

The strongest CO peak (region D1) contains 2.7–3.0 × $10^9 M_\odot$ of H_2, while $\sim 80\%$ of this quantity is located in the region closest to the galaxy center (region D2). The amount of molecular gas slightly decreases going south (region D3). It is interesting to note that the D2 region is not coincident with the AGN position (located at $23:36:25.0, + 21:09:02.5$, from Radovich et al. 2019), meaning that the peak of the CO flux is displaced with respect to the active nucleus. The three concentrations (regions NT1, NT2, and NT3) seen west from the galaxy disk have different contents of molecular gas: while the northern one (region NT1) has 4–7 × $10^8 M_\odot$ of H_2, moving south the molecular gas mass increases, but these regions are intrinsically larger with respect to the NT1 region, where our 2D fit found a very thin ellipse. Within the largest
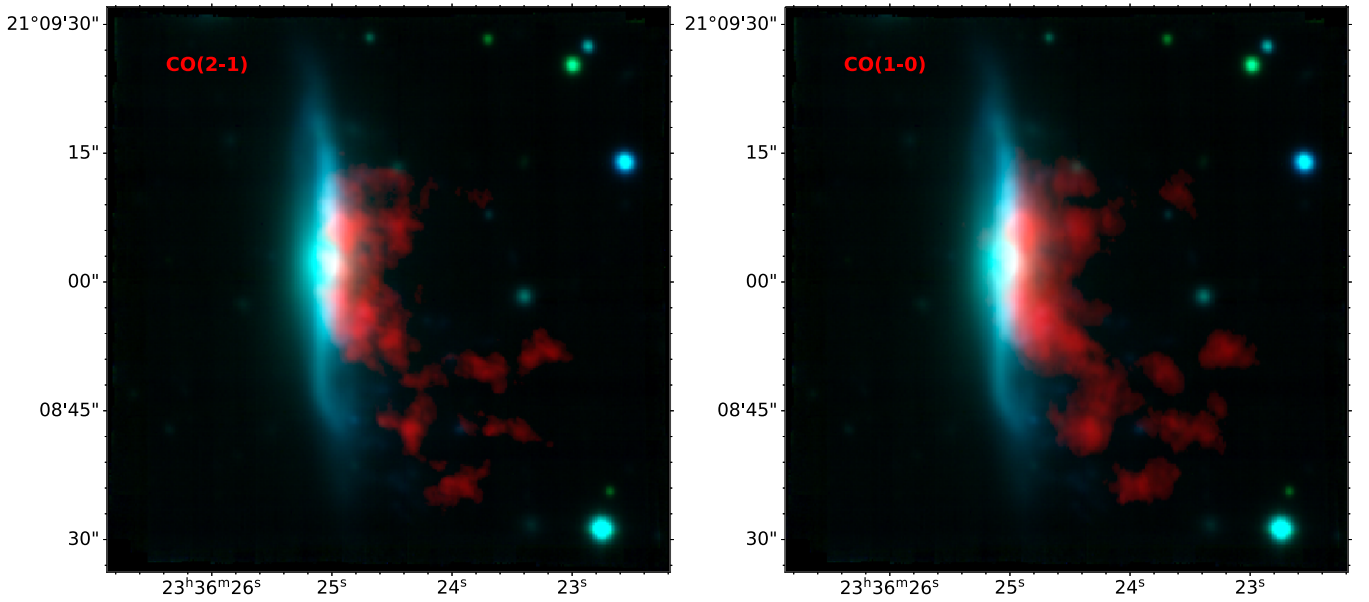
Figure 8. RGB images of JW100 obtained using the *V*- (in blue) and *I*-band (in green) images extracted from the MUSE data cube, and the CO emission as the red channel: left panel is made with the CO(2–1), right panel with the CO(1–0).

CO-emitting regions in the tail, we identified with our procedure five emitting blobs (FT1 to FT5), with masses (within the ellipses) above $\sim 1 \times 10^7$ and reaching $\sim 3 \times 10^8 M_\odot$. With our spatial and mass resolution, we cannot say whether our complexes are made of Milky Way–like GMCs (Solomon et al. 1987).

6. Resolved SFE

Having estimated the overall characteristics of the molecular gas in JW100, we now move on to the comparison of the ALMA and MUSE results, i.e., we correlate here the star formation measured through the Hα emission from MUSE data and the mass of molecular gas.

Figure 8 shows the RGB images obtained using the *V*- and *I*-band images extracted from the MUSE data cube and the CO zero moments from ALMA. The blue/green emission traces therefore the contribution of stars from MUSE, while the red regions show where the molecular gas is located. In particular, it can be seen how the molecular gas distribution in the disk is restricted to a region of ~ 20 kpc, while stars are distributed over larger scales. Moreover, the CO is totally displaced toward the west side of the galaxy, as described in previous sections. Finally, it seems to avoid the very central region where there is a hint of the cavity/ring described in Section 3.1.

In order to derive the SFEs over the 1 kpc scale covered by both the MUSE data and by the ALMA beam, we first convolve them to the same resolution and regrid them to the same WCS grid.

As for the MUSE results, we analyzed the spectra by measuring the emission-line fluxes on the stellar-continuum-subtracted data cubes and corrected them for the dust contribution using the Balmer decrement (Poggianti et al. 2017b). We then converted the Hα flux into the SFR adopting the Chabrier (2003) IMF using the relation given in Poggianti et al. (2017b). We then convolved the MUSE data (which have a $1''$ PSF) to the ALMA beam ($1{.}''4 \times 1{.}''1$, with PA = 33 deg). This allowed us to estimate the Σ_{SFR} shown in the upper-left panel of Figure 9 for the MUSE spaxels that have

been classified as star-forming according to the Baldwin–Phillips–Terlevich diagram (Baldwin et al. 1981) involving the N II line.

We then converted ALMA fluxes into mass densities, using Equation (1), and then regridded them onto the MUSE frame conserving the flux. This produces the H_2 mass density image shown in the upper-middle panel of Figure 9.

Given that the two frames are now convolved to the same beam/point-spread function (PSF) and have the same pixel size, it is straightforward to construct the depletion time (i.e., the time needed to consume the available molecular gas at the given measured SFR) map, shown in the upper rightmost panel of Figure 9, where we have also superimposed the stellar contour, as in previous maps.

Depletion times in JW100 range from $\sim 10^9$ yr in the eastern edge of the disk to $\sim 10^{10}$ yr in the tail, showing a clear gradient moving toward the west. The average depletion time in the disk regions (D1, D2, and D3) is 6.6 Gyr and becomes longer in the narrow tail regions (NT1, NT2, and NT3), where it reaches 7.3 Gyr. The FT regions in the far tail have depletion times longer than the Hubble time (13.9 Gyr on average).

Interestingly enough, the depletion times are generally larger than the typical value of ~ 2 Gyr (Bigiel et al. 2011) even in the central region, confirming that the ram pressure is also influencing the molecular gas located in the galaxy disk. The molecular gas velocity dispersion shown in Figure 1 is indeed high within the galaxy disk, with values that go from ~ 60 to more than 100 km s^{-1}, which are much higher than the typical values found in nearby galaxies (Wisnioski et al. 2012). Varying depletion times in disturbed galaxies are found in other nearby galaxies (Tomičić et al. 2018) on 0.5 kpc scales, and long depletion times (larger than 10 Gyr) are also common in the external part of disk galaxies (Bigiel et al. 2010).

The lower panel of Figure 9 shows the SFR density against the H_2 mass density for each pixel (black dots) and the average value found within each of the analyzed region as colored symbols. Red dashed lines are fixed depletion times, while the blue dashed line is the one derived from the 30 nearby disk galaxies of the HERACLES survey by Bigiel et al. (2011) at
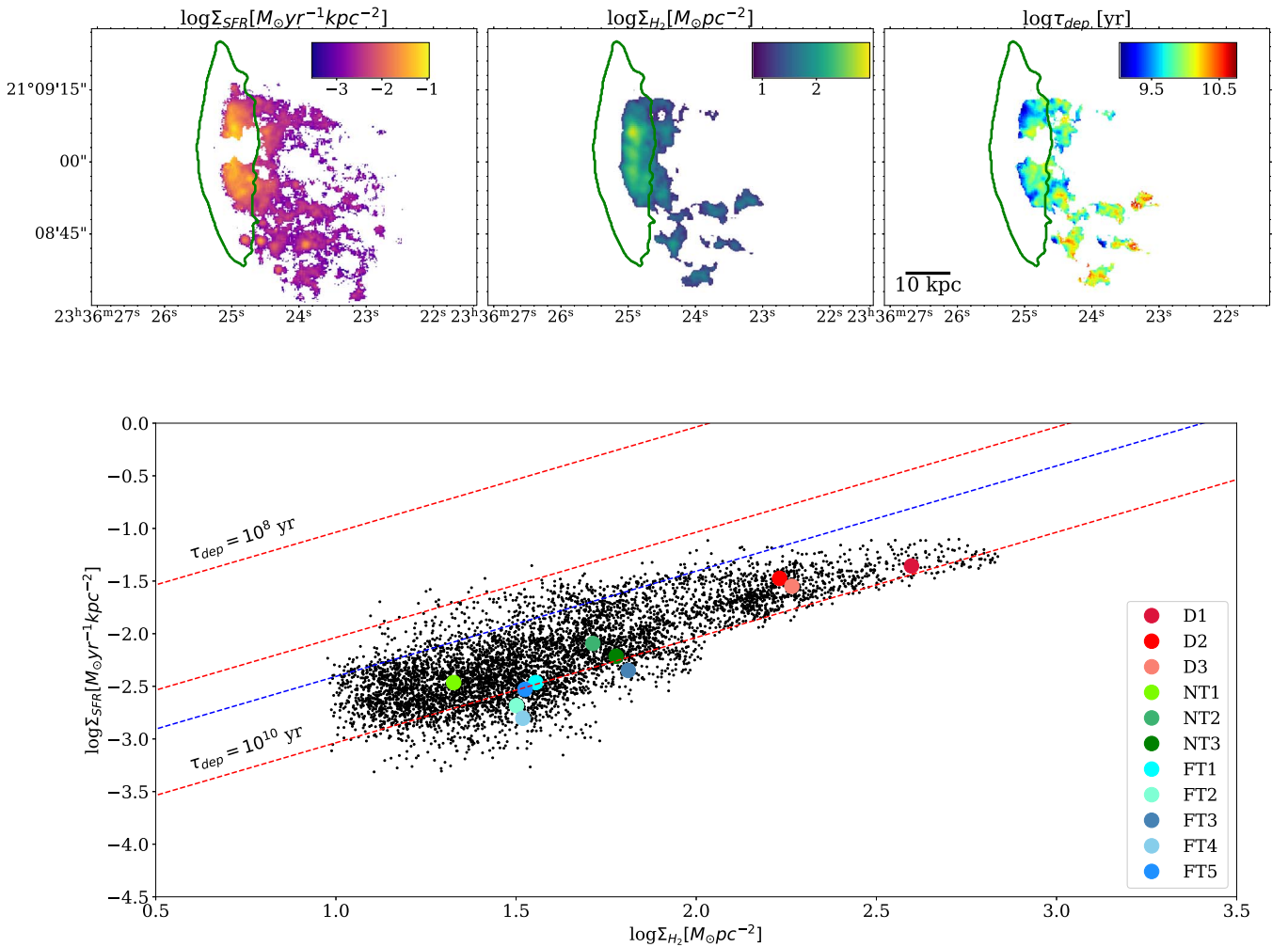
Figure 9. In the upper row: (left) map of the SFR density of spaxels classified as star-forming in MUSE (according to the N II lines); (middle) map of the molecular gas mass density as derived from ALMA CO(2–1) data; (right) map of the corresponding depletion time. In the lower row: star formation rate densities against molecular gas mass densities pixel by pixel (in black) and averaged values for the analyzed region (colored symbols). The red dashed lines are fixed depletion times (10^8, 10^9, and 10^{10} yr from top to bottom, respectively), while the blue dashed line is the average relation from Bigiel et al. (2011).

1 kpc scale resolution. The red dots, corresponding to regions D1, D2, and D3 located within the disk, lie below the local galaxies relation (in blue), i.e., they show low SFE. This confirms that this galaxy is forming new stars in the disk at a very low rate (see also Vulcani et al. 2018), given that the measured values of Σ_{H_2} are those typically found in galaxy bulges (Fisher et al. 2013). Lower values of α_{CO} (5–10 times lower than the Milky Way value adopted here) have been found in the central part of some HERACLES galaxies (Sandstrom et al. 2013), but only in the central kiloparsec, while regions D1, D2, and D3 span a larger extent of the galaxy disk. In particular, the central kiloparsec is dominated by AGN-like line ratios (Poggianti et al. 2017a; Radovich et al. 2019), according to different indicators (Poggianti et al. 2019a), and we therefore excluded it from the calculation. Our data confirm that local conditions play an important role in determining the star formation process, as already shown in the nearby galaxy M51 (Bigiel et al. 2016), and in 29 other nearby galaxies where dense gas tracers were available (Usero et al. 2015). Ram pressure then works in JW100 by enhancing the gas density in the disk and at the same time suppressing the global SFR, resulting in long depletion times both in the tail and in the galaxy disk (as already suggested in Moretti et al. 2018a).

Whether this is accompanied also by an enhancement of the molecular gas fraction, as in Nehlig et al. (2016), cannot be stated yet. Ongoing H I observations with MeerKAT will shed light on this issue. It is worth noticing, though, that in the GASP jellyfish galaxy JO206, the H I depletion time turned out to be shorter than expected (Ramatsoku et al. 2019), showing the opposite trend with respect to the molecular gas in JW100.

In the region in which we detect the ring, we measure both high gas densities and low SFE, possibly due to the fact that molecular gas within that region is gravitationally unbound, and therefore less prone to become dense and form new stars (Momose et al. 2010; Sorai et al. 2012; Maeda et al. 2018). It has been suggested, in fact, that high-mass galaxies, or galaxies with high molecular gas fraction, may have longer depletion times (Leroy et al. 2013).

7. Conclusions

In this paper, we presented the first results of an ongoing ALMA campaign devoted to studying the complex baryon cycle that leads to the quenching of the star formation in galaxies subject to ram pressure stripping in the dense cluster environment. Our targets, among which is the JW100 galaxy here

analyzed, are galaxies belonging to clusters at redshift ~0.05 and are part of the GASP project (Poggianti et al. 2017b).

JW100 is the first not nearby jellyfish galaxy for which we can confirm the presence of molecular gas out to large distances from the galaxy center, thanks to the ALMA data over scales comparables to those of optical data (i.e., ~1 kpc). Only recently has ALMA been used to confirm single-dish results by Jáchym et al. (2019) for the much more nearby jellyfish galaxy ESO 137–001 in the Norma cluster.

Our ALMA data reveal the presence of $\sim 2.5 \times 10^{10} M_\odot$ of molecular gas (lower limit), i.e., ~8% of the galaxy stellar mass, a value that is at least eight times the one found in the local xCOLD GASS sample (Saintonge et al. 2017) and in the Virgo cluster galaxies (Corbelli et al. 2012) for galaxies of similar mass. The measured scatter in both samples cannot explain our measurements. JW100 is therefore extremely rich in molecular gas, suggesting that part of it is newly formed as a consequence of the gas stripping. In fact, ~30% of the molecular gas that we measure is located in the stripped tail and could be newly formed there from the stripped neutral gas or from the diffuse molecular gas.

In JW100, the CO emission resolved by ALMA 12 m, combined with the ACA, is able to completely recover the APEX fluxes within the measurement errors when considering the same velocity range.

To understand on what scales the molecular gas is diffuse, we remind readers here that the largest recoverable scales of ALMA 12 m array and ALMA+ACA are $7''.5$ and $18''$, respectively (see Section 2), which convert to ~8 and ~19 kpc at the cluster distance. Our data, therefore, suggest that 57% of the molecular gas in the disk is concentrated on scales up to 8 kpc, while only 30% of it is in the same conditions in the tail, demonstrating that the cold gas in the tail is more diffuse than that in the disk (Pety et al. 2013; Jáchym et al. 2019).

The molecular gas within the galaxy disk is totally displaced with respect to the stellar component, demonstrating that the molecular gas reservoir of JW100 is disturbed by the ram pressure exerted by the hot ICM on the galaxy while it falls toward the cluster center. A clear double component in the CO emission is detected in the D1 northern disk region, where molecular gas is accumulated due to the geometry of the system with respect to the infalling galaxy. Molecular gas is also found in the galaxy tail, broadly cospatial with the ionized gas distribution and with the same kinematics.

The total mass of cold gas in the tail is $\sim 7 \times 10^9 M_\odot$ and appears concentrated in large regions with sizes of a few kiloparsecs. The most massive regions outside the stellar disk are close to the disk itself (~1–2 kpc), but the farthest CO-emitting regions are located at more than 35 kpc from the galaxy center, a distance that again suggests the formation of molecular gas in situ from the stripped H I gas or diffuse molecular gas. This has been also suggested by the recent study by Jáchym et al. (2019) on the nearby jellyfish galaxy ESO 137–001, on the basis of CO(2–1) ALMA data.

Our data set also includes ALMA band 3 data, i.e., the CO(1–0) line emission, which have allowed us to measure the line temperature ratio (r_{21}). The r_{21} ratio is within expectations in the galaxy disk, where it shows values from 0.2 to 1, with an average value of 0.58 (lower than the usual adopted value of 0.7–0.8). The regions located well outside the galaxy disk tend, instead, to show higher values. The high values of the r_{21} ratio in the farther FT regions, together with their low velocity dispersion and the presence of a single emission-line

component lead us to conclude that they are composed by dense star-forming molecular gas. The comparison between the typical lifetime of a dense molecular gas cloud and the time needed to reach such distances along the stripped tail strongly supports the scenario in which these clouds are formed in situ, either from stripped neutral gas or from stripped diffuse molecular gas. The nearby clumps, instead, might bear the trace of a secondary, less dense, molecular gas component that has been stripped from the disk (see the narrow tail NT3 region, for example).

The total amount of molecular gas, coupled with its distribution, kinematics, and physical conditions, suggest that the molecular gas content of this galaxy is increased with respect to undisturbed galaxies of similar mass, and that this is probably due to the newly formed gas that we see in the tail coupled with an enhancement of molecular gas also within the disk.

By coupling the ALMA data and the GASP results obtained from MUSE spectra, we finally derive the SFE over scales of 1 kpc, for the first time in a distant jellyfish galaxy. We find that there is a clear gradient in the depletion time, with average values that go from ~6 Gyr within the disk to ~14 Gyr in the farthest tail regions (FT1–FT5). Most of the molecular gas in the tail, therefore, will not be used to fuel the SF, but will ultimately join the ICM. The high value that we find even within the galaxy disk can be explained by an increased turbulence caused either by the bar or by the ram pressure itself, which would make the gas unable to adequately form stars. This mechanism has also been proposed to explain the star formation quenching at the center of our own Galaxy (Haywood et al. 2016) and in various regions in M51 (Querejeta et al. 2019), where the SFE has been found to be related to turbulent motions and galactic dynamics. Both dedicated simulations of gas-rich galaxies (Khoperskov et al. 2018) and isolated galaxies with central spheroids with stellar mass densities larger than $\sim 3 \times 10^8 M_\odot$ (Gensior et al. 2019) have confirmed this result. The comparison between ALMA 12 m and APEX data also suggests that a significant amount of CO is diffuse on scales larger than the one recoverable with ALMA 12 m, implying that the molecular gas densities might be even higher (especially in the tail), making the SFE consistently lower.

Further analysis on the three other GASP galaxies for which ALMA data are already available (JO201, JO204, JO206) will help in clarifying the effect of the ram pressure stripping on this issue.

ORCID iDs

Alessia Moretti ⍟ https://orcid.org/0000-0002-1688-482X
Rosita Paladino ⍟ https://orcid.org/0000-0001-9143-6026
Bianca M. Poggianti ⍟ https://orcid.org/0000-0001-8751-8360
Paolo Serra ⍟ https://orcid.org/0000-0001-5965-252X
Elke Roediger ⍟ https://orcid.org/0000-0003-2076-6065
Marco Gullieuszik ⍟ https://orcid.org/0000-0002-7296-9780
Neven Tomičić ⍟ https://orcid.org/0000-0002-8238-9210
Mario Radovich ⍟ https://orcid.org/0000-0002-3585-866X
Benedetta Vulcani ⍟ https://orcid.org/0000-0003-0980-1499
Yara L. Jaffé ⍟ https://orcid.org/0000-0003-2150-1130
Jacopo Fritz ⍟ https://orcid.org/0000-0002-7042-1965
Daniela Bettoni ⍟ https://orcid.org/0000-0002-4158-6496
Mpati Ramatsoku ⍟ https://orcid.org/0000-0003-0231-3249
Anna Wolter ⍟ https://orcid.org/0000-0001-5840-9835

References

Abramson, A., Kenney, J. D. P., Crowl, H. H., et al. 2011, AJ, 141, 164
Bacon, R., Accardo, M., Adjali, L., et al. 2010, Proc. SPIE, 7735, 773508
Baldwin, J. A., Phillips, M. M., & Terlevich, R. 1981, PASP, 93, 5
Bellhouse, C., Jaffé, Y. L., Hau, G. K. T., et al. 2017, ApJ, 844, 49
Bigiel, F., Leroy, A. K., Jiménez-Donaire, M. J., et al. 2016, ApJL, 822, L26
Bigiel, F., Leroy, A. K., Walter, F., et al. 2011, ApJL, 730, L13
Bigiel, F., Walter, F., Blitz, L., et al. 2010, AJ, 140, 1194
Biviano, A., Moretti, A., Paccagnella, A., et al. 2017, A&A, 607, A81
Bolatto, A. D., Wolfire, M., & Leroy, A. K. 2013, ARA&A, 51, 207
Bolatto, A. D., Wong, T., Utomo, D., et al. 2017, ApJ, 846, 159
Braine, J., & Combes, F. 1992, A&A, 264, 433
Casasola, V., Hunt, L. K., Combes, F., García-Burillo, S., & Neri, R. 2011, A&A, 527, A92
Casoli, F., & Dupraz, C. C. F. K. I. 1991, A&A, 251, 1
Catinella, B., Saintonge, A., Janowiecki, S., et al. 2018, MNRAS, 476, 875
Chabrier, G. 2003, PASP, 115, 763
Chevance, M., Kruijssen, J. M. D., Hygate, A. P. S., et al. 2019, MNRAS, in press
Chung, A., van Gorkom, J. H., Kenney, J. D. P., Crowl, H., & Vollmer, B. 2009, AJ, 138, 1741
Cicone, C., Maiolino, R., Sturm, E., et al. 2014, A&A, 562, A21
Consolandi, G., Gavazzi, G., Fossati, M., et al. 2017, A&A, 606, A83
Corbelli, E., Bianchi, S., Cortese, L., et al. 2012, A&A, 542, A32
Dumke, M., & Mac-Auliffe, F. 2010, Proc. SPIE, 7737, 77371J
Feruglio, C., Fiore, F., Carniani, S., et al. 2015, A&A, 583, A99
Fisher, D. B., Bolatto, A., Drory, N., et al. 2013, ApJ, 764, 174
Fossati, M., Fumagalli, M., Boselli, A., et al. 2016, MNRAS, 455, 2028
Fritz, J., Moretti, A., Gullieuszik, M., et al. 2017, ApJ, 848, 132
Fumagalli, M., Fossati, M., Hau, G. K. T., et al. 2014, MNRAS, 445, 4335
Funes, J. G., Corsini, E. M., Cappellari, M., et al. 2002, A&A, 388, 50
Gensior, J., Kruijssen, J. M. D., & Keller, B. W. 2019, MNRAS, submitted
George, K., Poggianti, B. M., Gullieuszik, M., et al. 2018, MNRAS, 479, 4126
Gitti, M. 2013, MNRAS, 436, L84
Gullieuszik, M., Poggianti, B. M., Moretti, A., et al. 2017, ApJ, 846, 27
Gunn, J. E., & Gott, J. R. I. 1972, ApJ, 176, 1
Haywood, M., Lehnert, M. D., Di Matteo, P., et al. 2016, A&A, 589, 66
Helfer, T. T., Thornley, M. D., Regan, M. W., et al. 2003, ApJS, 145, 259
Helfer, T. T., Vogel, S. N., Lugten, J. B., & Teuben, P. J. 2002, PASP, 114, 350
Heyer, M., & Dame, T. 2015, ARA&A, 53, 583
Ignesti, A., Gitti, M., Brunetti, G., et al. 2018, A&A, 610, A89
Ignesti, A., Gitti, M., Brunetti, G., Feretti, L., & Giovannini, G. 2017, A&A, 604, A21
Jáchym, P., Combes, F., Cortese, L., Sun, M., & Kenney, J. D. P. 2014, ApJ, 792, 11
Jáchym, P., Kenney, J. D. P., Sun, M., et al. 2019, ApJ, 883, 145
Jáchym, P., Sun, M., Kenney, J. D. P., et al. 2017, ApJ, 839, 15
Jaffé, Y. L., Poggianti, B. M., Moretti, A., et al. 2018, MNRAS, 476, 4753
Jaffé, Y. L., Smith, R., Candlish, G. N., et al. 2015, MNRAS, 448, 1715
Jogee, S., Scoville, N., & Kenney, J. D. P. 2005, ApJ, 630, 837
Kaneko, H., Kuno, N., Iono, D., et al. 2017, PASJ, 69, 66
Kenney, J. D. P., van Gorkom, J. H., & Vollmer, B. 2004, AJ, 127, 3361
Khoperskov, S., Haywood, M., Di Matteo, P., Lehnert, M. D., & Combes, F. 2018, A&A, 609, 60
Kuno, N., Sato, N., Nakanishi, H., et al. 2007, PASJ, 59, 117
Kuzio de Naray, R., Zagursky, M. J., & McGaugh, S. S. 2009, AJ, 138, 1082
Lee, B., & Chung, A. 2018, ApJ, 866, 10
Lee, B., Chung, A., Tonnesen, S., et al. 2017, MNRAS, 466, 1382
Leroy, A. K., Walter, F., Bigiel, F., et al. 2009, AJ, 137, 4670
Leroy, A. K., Walter, F., Sandstrom, K., et al. 2013, AJ, 146, 19
Machacek, M. E., Nulsen, P., Stirbat, L., Jones, C., & Forman, W. R. 2005, ApJ, 630, 280
Maeda, F., Ohta, K., Fujimoto, Y., Habe, A., & Baba, J. 2018, PASJ, 70, 37
McMullin, J. P., & Waters, B. S. D. Y. W. G. K. 2007, in ASP Conf. Ser. 376, Astronomical Data Analysis Software and Systems XVI, ed. F. H. R. A Shaw & D. J. Bell (San Francisco, CA: ASP), 127
Merluzzi, P., Busarello, G., Dopita, M. A., et al. 2013, MNRAS, 429, 1747
Miyamoto, Y., Nakai, N., Seta, M., et al. 2017, PASJ, 69, 83
Momose, R., Okumura, S. K., Koda, J., & Sawada, T. 2010, ApJ, 721, 383
Moretti, A., Paladino, R., Poggianti, B. M., et al. 2018a, MNRAS, 480, 2508
Moretti, A., Poggianti, B. M., Gullieuszik, M., et al. 2018b, ApJ, 475, 4055
Nehlig, F., Vollmer, B., & Braine, J. 2016, A&A, 587, A108
Nieten, C., Neininger, N., Guélin, M., et al. 2006, A&A, 453, 459
Nishimura, A., Tokuda, K., Kimura, K., et al. 2015, ApJS, 216, 18
Noordermeer, E., Van Der Hulst, J. M., Sancisi, R., Swaters, R. S., & Van Albada, T. S. 2007, MNRAS, 376, 1513
Oosterloo, T., & van Gorkom, J. 2005, A&A, 437, L19
Peñaloza, C. H., Clark, P. C., Glover, S. C. O., Shetty, R., & Klessen, R. S. 2017, MNRAS, 465, 2277
Pety, J., Schinnerer, E., Leroy, A. K., et al. 2013, ApJ, 779, 43
Poggianti, B. M., Gullieuszik, M., Tonnesen, S., et al. 2019a, MNRAS, 482, 4466
Poggianti, B. M., Ignesti, A., Gitti, M., et al. 2019b, ApJ, 887, 155
Poggianti, B. M., Jaffé, Y. L., Moretti, A., et al. 2017a, Natur, 548, 304
Poggianti, B. M., Moretti, A., Gullieuszik, M., et al. 2017b, ApJ, 844, 48
Price-Whelan, A. M., Sipőcz, B. M., Günther, H. M., et al. 2018, AJ, 156, 123
Querejeta, M., Schinnerer, E., Schruba, A., et al. 2019, A&A, 625, A19
Radovich, M., Poggianti, B., Jaffé, Y. L., et al. 2019, MNRAS, 486, 486
Ramatsoku, M., Serra, P., Poggianti, B. M., et al. 2019, MNRAS, 487, 4580
Riener, M., Kainulainen, J., Henshaw, J. D., et al. 2019, A&A, 628, 78
Robitaille, T. P., Tollerud, E. J., Greenfield, P., et al. 2013, A&A, 558, 33
Saintonge, A., Catinella, B., Tacconi, L. J., et al. 2017, ApJS, 233, 22
Saintonge, A., Kauffmann, G., Kramer, C., et al. 2011, MNRAS, 415, 32
Sandstrom, K. M., Leroy, A. K., Walter, F., et al. 2013, ApJ, 777, 5
Schinnerer, E., Meidt, S. E., Pety, J., et al. 2013, ApJ, 779, 42
Scott, T. C., Brinks, E., Cortese, L., Boselli, A., & Bravo-Alfaro, H. 2018, MNRAS, 475, 4648
Serra, P., Jurek, R., & Flöer, L. 2012, PASA, 29, 296
Serra, P., Westmeier, T., Giese, N., et al. 2015, MNRAS, 448, 1922
Sheth, K., Vogel, S. N., Regan, M. W., Thornley, M. D., & Teuben, P. J. 2005, ApJ, 632, 217
Solomon, P., & Vanden Bout, P. 2005, ARA&A, 43, 677
Solomon, P. M., Rivolo, A. R., Barrett, J., & Yahil, A. 1987, ApJ, 319, 730
Sorai, K., Kuno, N., Nishiyama, K., et al. 2012, PASJ, 64, 51
Sorai, K., Nakai, N., Kuno, N., Nishiyama, K., & Hasegawa, T. 2000, PASJ, 52, 785
Sun, M., Donahue, M., Roediger, E., et al. 2010, ApJ, 708, 946
Sun, M., Donahue, M., & Voit, G. M. 2007, ApJ, 671, 190
Tomičić, N., Hughes, A., Kreckel, K., et al. 2018, ApJL, 869, L38
Usero, A., Leroy, A. K., Walter, F., et al. 2015, AJ, 150, 115
Verdugo, C., Combes, F., Dasyra, K., Salomé, P., & Braine, J. 2015, A&A, 582, A6
Vulcani, B., Poggianti, B. M., Gullieuszik, M., et al. 2018, ApJL, 866, L25
Watson, L. C., & Koda, J. 2017, ASSL, 434, 175
Wisnioski, E., Glazebrook, K., Blake, C., et al. 2012, MNRAS, 422, 3339